Experimental investigation of cavitation-induced erosion around a surface-mounted bluff body

Wear 480-481 (2021) 203917

Contents lists available at ScienceDirect

Wear

journal homepage: www.elsevier.com/locate/wear

Experimental investigation of cavitation-induced erosion around a surface-mounted bluff body

Saad Jahangir [a,*], Ebrahim Ghahramani [b], Magdalena Neuhauser [c], Sébastien Bourgeois [c], Rickard E. Bensow [b], Christian Poelma [a]

[a] Department of Process & Energy (Faculty 3mE), Delft University of Technology, 2628 CA, Delft, the Netherlands
[b] Mechanics and Maritime Sciences, Chalmers University of Technology, 412 96, Gothenburg, Sweden
[c] R&D Department, ANDRITZ Hydro, 1800, Vevey, Switzerland

ARTICLE INFO

Keywords:
Cavitation erosion
Vortex shedding
Semi-circular cylinder
Bluff body
Paint test

ABSTRACT

The objective of this study is to investigate the collapsing behavior of cavitation, which leads to the erosion of material. An experimental examination was conducted in a channel with a semi-circular cylinder obstacle, which serves as a "vortex cavity" generator. Cavitation was achieved by employing a range of pressure differences over the test section and a high-speed camera was used to observe the cavitation behavior. The flow field behind the semi-circular cylinder was investigated as a characteristic example of bluff bodies that exhibit a distinct, separated vortex flow in their wake. The cases with the bluff body were also compared to the ones without the bluff body. Erosion tests were performed using paint (stencil ink). The intensity of cavitation is characterized by the cavitation number (σ); the lower the cavitation number, the higher the cavitation intensity. The erosion (removal of paint) after 40 min of operation revealed distinct and repeatable results. For a high cavitation number, a large number of von Karman-vortex-like cavities are shed downstream of the obstacle. This results in a higher number of collapse events and, ultimately, more erosion. On the other hand, at lower cavitation numbers, the erosion took place at the cavity's closure line. It was seen that with the increase in cavitation intensity, the erosion area increases. Moreover, the bluff body obstacle promotes and localizes cavitation-induced erosion on the sample plate compared to the cases without the bluff body. This ultimately means that in the cases with the bluff body, less power is required in the system to cause erosion. The erosion patterns caused by the bluff body cavitation are more repeatable compared to the cases without the bluff body due to the localized cavitation load. The erosion pattern from the paint test is also compared with a material loss test (30 h of operation). A very good qualitative agreement is found between the two tests, with the paint test requiring approximately two orders of magnitude less running time of the facility. We demonstrate that paint tests, combined with this geometry, provide an efficient and economical way to investigate erosion patterns compared to expensive material loss tests.

1. Introduction

Cavitation is a phenomenon in which liquid converts to vapor due to the drop of the local liquid pressure below the vapor pressure. Cavitation can occur at micro scales as well as at macro scales. Examples include diesel injection nozzles [1], gear pumps [2], turbines [3] and pumps [4]. In practical applications, the presence of cavitation in hydraulic systems, which are designed for homogeneous flows, is viewed as a nuisance for many reasons, in particular yielding lower efficiency and wear. Although cavitation is harmful in many engineering applications, it can be useful in others such as ultrasonic cleaning [5] and biomedical treatment [6].

Among all unfavorable consequences of cavitation, surface erosion is the most complex. Surface erosion is one of the most studied topics in the field of cavitation, as it has a drastic impact on surfaces and devices over time, and poses a severe limitation in the design and operation. The first comprehensive study on the collapse of an empty cavity at a rigid wall was performed by Plesset and Chapman [7]. These theoretical results were experimentally verified by Lauterborn and Bolle [8]. Dular et al. [9] presented the development of an erosion pit (footprint of erosion

* Corresponding author. Present address: Department of Energy and Process Engineering, Norwegian University of Science and Technology, Trondheim, 7491, Norway.
E-mail address: saad.jahangir@ntnu.no (S. Jahangir).

https://doi.org/10.1016/j.wear.2021.203917
Received 20 September 2020; Received in revised form 13 March 2021; Accepted 7 April 2021
Available online 21 May 2021

caused by collapse events) on a foil. The authors pointed out that the foil is damaged various times before a hole is ultimately pierced. It was inferred that single large pits were created from numerous impacts of shock waves in the same area. The collapse of a vapor bubble or vapor cloud may induce a shock wave and a high-speed micro-jet, which can cause erosion [10,11]. In the literature, the most common mechanism causing cavitation erosion is the micro-jet phenomenon [12]. This is a complex problem as it includes both material and hydrodynamic aspects. Various studies have been performed to characterize cavitation and prevent its undesirable effects on the full-scale applications (e.g., Refs. [13,14]).

Material properties such as hardness and yield strength also contribute significantly to the damage caused by cavitation [15]. Hanke et al. [16] analyzed cavitation erosion on different coatings and substrates by means of optical and electron microscopy. The authors concluded that the resistance of coated layers against cavitation erosion is higher than that of the cast materials and incubation erosion time is about twice as long. Gao and Zhang [17] analyzed cavitation erosion evolution on stainless steel. Early cavitation erosion in microstructure was studied together with the evolution of roughness, hardness and residual stress. Although these studies show the extent of damage caused by cavitation, cavitation mechanisms that cause this erosion are not linked due to lack of optical access. On the other hand, variation in liquid properties can also influence the cavitation erosion. Liu et al. [18] evaluated the influence of liquid properties on cavitation erosion resistance of the copper alloy. Deionized water, tap water and 3.5 wt% NaCl solution were used as working liquids. Tap water was found to be most erosive. However, in practical applications, the working liquid cannot be changed most of the time.

Despite an extensive available collection of experimental studies on cavitation, studies that link cavitation to erosion are limited. The main reason is the lack of effective experimental techniques to capture the very fast cavitation collapses (in the order of microseconds), together with a very slow erosion process (in the order of several days). Due to challenges in measuring the pressure peaks caused by bubble implosions using commercial pressure transducers, it is not possible to determine the aggressiveness of cavitation erosion precisely [19]. A possible option is the numerical simulation approach. Computational Fluid Dynamics (CFD) can give detailed information of the flow field which helps to further understand the cavitation regime and identify the more aggressive structures. For instance, Ji et al. [20] investigated the formation of cavitating flow around a twisted hydrofoil and revealed that cavitation promotes vortex production and increases unsteadiness in the flow. Furthermore, it was demonstrated in recent studies (e.g. Refs. [21–23]) that Large Eddy Simulation (LES) is a promising approach for studying unsteady cavitating flows that can reproduce the cavitation-vortex interaction. In order to numerically predict cavitation erosion several methodologies have been presented in the literature. However, while there are various CFD methods to model cavitation dynamics (see e.g. Ref. [24], and the references therein), a well-developed erosion model that can relate the cavitation dynamics to the rate of material loss is still missing. Eskilsson et al. [25] reviewed three different categories of models and found that none of them were able to reproduce the experimental results of cavitation erosion over a NACA0015 foil. The applied methods were: (1) the discrete bubble model that estimates erosiveness by computing the pressure inside advected microscopic bubbles; (2) the gray level method that relates the standard deviation of vapor fraction to the erosive energy; and (3) the intensity function method which uses the time derivative of the pressure to correlate the erosion intensity. Also, a homogeneous mixture model was used to represent the two-phase flow in all of the simulations, while the turbulence was modeled using an implicit LES approach. Nevertheless, Eskilsson et al. [25] suggested that if a micro-bubble model is coupled with the common mixture models for the macro scale cavities, one can estimate the erosion intensity by resolving the collapsing bubble dynamics at the micro-scale. In the same trend, recently Peters and el Moctar [26] developed an erosion model based on a hybrid Eulerian mixture - Lagrangian bubbles algorithm (similar to the one by Ref. [27]) and they could correlate the maximum collapse radii of bubbles with diameters of measured erosion pits. In another recent study, Joshi et al. [28] coupled the bubble collapse and material response in detail for the first time. They used a Smoothed Particle Hydrodynamics solver and took into account the complex fluid-structure interaction.

As another alternative, scaled experiments are utilized for the risk evaluation of probable erosive full-scale conditions and validation of numerical models [29]. For this purpose, different test geometries are used to study and investigate cavitation in laboratories [30–32]. Among these geometries, cavity structures around a bluff body are considerably more aggressive and more erosive compared with hydrofoils and wedges. A 3D bluff body can generate strong cavitating vortices that collapse on a narrow region in the wake of the obstacle, which in turn can induce severe localized erosion. Saito and Sato [33] investigated the cavitation collapse behind a circular cylinder and the erosion on an aluminum plate behind the cylinder. They observed that near the channel wall, the cavities collapse rapidly with a colliding motion towards the wall. In the symmetrical test section, these collapses had different patterns, such as radial collapse and axial collapse. Saito and Sato [33] also concluded that the occurrence frequency of high impacts causing the cavitation damage pits is much smaller than the number of passing cavities which means that not each shedding cycle creates a ‘high-impact event’. Fry [34] studied the cavity wake dynamics for a circular cylinder and measured the noise spectra in the downstream region behind the cylinder. From the measured noise spectra, he concluded that peak collapse intensity occurs at the end of the cyclic collapse process when the collapsing cavities are as large as possible without affecting the cyclic process. The peak collapse intensity produces maximum noise and maximum erosion rate.

An important feature in the erosivity of a bluff body is the cross-section of the body and the corresponding flow dynamics in the wake area. Escaler et al. [35] mounted four different obstacles on the flat suction side of a hydrofoil to alter the flow field and accelerate the erosion process. They found the flat-front semi-circular cylinder to be the most suitable geometry for generating a reproducible pitting on the sample plate within a short period of time. By observing severe localized erosion, in a following study, Escaler et al. [36] stated that cavitation vortices could maintain the presence of vapor very close to the surface during their collapse and their circulation is a significant parameter in their erosive power. Using an inlet velocity of 35 m/s at a cavitation number of 1, it took at least 75 h for Escaler et al. [36] to reach measurable cumulative cavitation damage in stainless steel. While dramatically cutting the duration of the experiment (compared to the case without an obstacle), these are still very expensive experiments.

Recently, we studied the dynamics of the cavitating flow around a semi-circular cylinder mounted on a surface in the throat of a converging-diverging channel [37]. The setup creates various 3D flow structures around the body at high Reynolds numbers. Based on the observed results, vortex shedding can have multiple patterns in cavitating flows. At higher cavitation numbers, the vortices are shed in a cyclic pattern. On the other hand, at very low cavitation numbers, large fixed cavities are formed in the wake area. Besides, at very low cavitation numbers, reverse flow is observed that moves upstream and causes the detachment of the whole cavity from the cylinder. Earlier studies at ANDRITZ Hydro have shown this flow to be erosive, and the erosion pattern varies as the flow rate is changed.

In this study, we investigate the cavitation erosion in the same test-rig as the earlier study [37] and compare the erosion patterns for different flow rates with and without the cylinder in the channel throat. This study is a major step forward from Ghahramani et al. [37] as we identify the erosive behavior of various cavitation events. There are many studies focused on the visual observation of the cavitating flows (e.g., Refs. [38,39]). However, in the current study, we combine high-speed visualization together with paint-removal to understand the

erosive nature of cavitation. A range of measurements has been performed to better understand the relationship between the physical phenomenon and potentially erosive impacts. While the high-speed video records visual events, such as cavitation collapse and rebound, the resulting erosion pattern is measured using paint tests. It will be shown that the paint test approach can significantly decrease the measurement period while it leads to similar erosion patterns as compared to earlier studies in the literature.

In the following sections, the test facility and experimental conditions are described first. After that, the experimental method and data processing are explained. Then, the obtained results are presented in detail, including a discussion about different erosion patterns and the effect of the bluff body. Finally, the paper is concluded with a summary of the main findings.

2. Methodology

2.1. Experimental setup

The experiments are conducted at the ANDRITZ high-speed erosion test-rig. The objective of the test-rig is to generate an aggressive cavitation regime in the wake of the bluff body. As shown in Fig. 1, the semi-circular cylinder is mounted at the end of a ramp surface, and a flat plate is put behind the cylinder. The plate is then painted to measure the erosion pattern. This simple setup of the body with the bottom surfaces is then put in a converging-diverging channel. A schematic overview of the flow setup utilized for the measurements, along with an enlarged view of the converging-diverging section, is depicted in Fig. 2. The flow in the loop system is driven by a pump (KSB 6N89-858-233) from an open water tank. The pump is placed approximately 1.98 m below the main feeding line to avoid cavitation. To have a considerable pressure drop and higher local velocities, which augments cavitation, the channel has a converging-diverging rectangular cross-section with dimensions of 74×54 mm^2. Then it is further contracted to a section of $25\times$ 54 mm^2 through a curved profile upper wall and a simple 45° slope on the lower wall, while the channel width is constant everywhere. The simple bottom slope is, in fact, the ramp surface before the cylinder (Fig. 1). Also, the flat plate has dimensions of 106×54 mm^2, and the cylinder has a diameter of 5 mm and a height of 9.65 mm (inspired by previous studies: Escaler et al. [36]; Ghahramani et al. [37]). The flat side of the cylinder is facing upstream, and at the attachment of the flat plate and the sloped wall, there is a small backward-facing step with a height of 0.5 mm. The feeding line of the experimental setup is a circular tube with a diameter of 114.3 mm; however, it is transformed into a rectangular section ($74\times$ 54 mm^2) through a converging tube at 140 cm before the main test section. The upstream length available for development is more than 100D, in order to have a fully-developed turbulent flow entering the test section. After the test section, the pressure in the flow is recovered in a pressure recovery section. At the end of the pressure recovery section, a valve is present to vary the global static pressure of the system. There are two outflow pipes, however only the second pipe is used during the tests.

The flow can be visualized through the sidewalls, which are made of Polymethyl methacrylate (PMMA). Also, two pressure transducers are used to measure the upstream (p_1) and downstream pressure (p_2), which

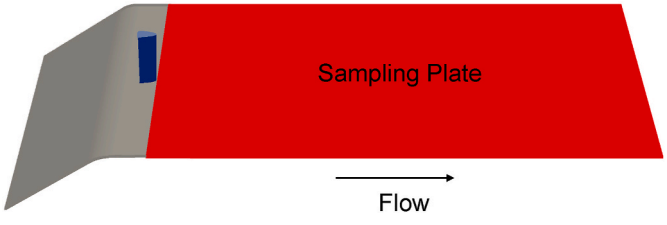

Fig. 1. Bluff body and the sampling plate. The sampling plate is painted to study erosion.

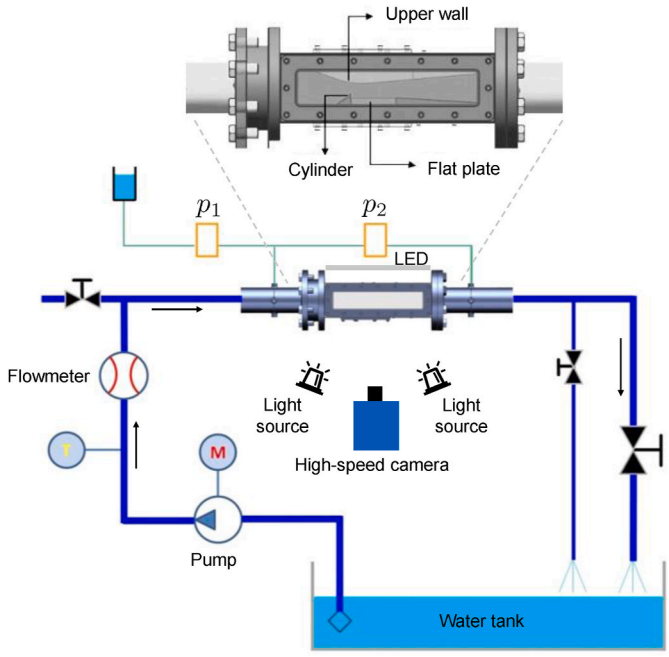

Fig. 2. Schematic overview of the experimental facility indicating different components together with an enlarged view of the test section (dimensions not to scale).

are located 380 mm before and 500 mm after the bluff body, respectively. Note that the time-averaged pressure measurements are used in this study. Before and after the measurements, water samples were taken to determine the gas content in the system using an oxygen sensor (RDO PRO-X Probe). As the volume of the water tank was large, no difference was seen in the oxygen measurements. The average dissolved oxygen content was 8.25 mg/L with negligible variation through the whole series of experiments. Finally, an electromagnetic flowmeter (DN 100 from ABB) is used to measure the volumetric flow rate. The measurement uncertainty for each of the pressure transducers as well as the flowmeter is ±0.15%. The measurements from the downstream pressure transducer, the flowmeter, and the temperature sensor[1] are utilized to determine the cavitation number σ,

$$\sigma = \frac{p_2 - p_v}{\frac{1}{2}\rho u_{th}^2}, \tag{1}$$

where p_v is the vapor pressure, ρ is the density of the fluid, and u_{th} is the area-averaged velocity (evaluated from the flowmeter) of the flow at the throat of the converging-diverging section without cylinder. The lower the cavitation number, the higher the cavitation intensity. Further details on the experimental setup can be found in Ghahramani et al. [37].

A high-speed camera (Phantom v411) with a field of view of 640 × 232 pixels was used for imaging. Two light sources from the front and an LED panel behind the measurement section were used to illuminate the cavitation phenomena. After trying different angles to find the best possible visualization, the camera was placed at an angle of 32° to the horizontal surface.

[1] The temperature measurement (20.59 °C - 20.69 °C) is used to calculate the vapor pressure by applying the Antoine equation. Note that the time-averaged temperature was used.

2.2. Painting the sample plate

For the paint tests, red stencil ink[2] (Wilson super ink, Wilson Sporting Goods Co.) was applied on the flat plate downstream of the cylinder uniformly and as thin as possible, using a syringe. Paint tests have been used before for erosion assessment of cavitating flows (see e.g. Refs. [40,41]). [40], showed that brush-on stencil inks could be good indicators of cavitation erosion and the uniformity of the applied ink does not severely affect its removal. Stencil ink has also been used in a recent study by Arabnejad et al. [42]. In the current study, we used a new approach for painting and applied the ink by a syringe. The ink is poured on the sample plate until its top surface is fully covered with ink and few drops drip out from the sides. This step causes the ink layer to have the same thickness and uniformity every time. In Fig. 3(a), a photograph of the sample plate can be seen during the application of the paint. The tests were conducted once the paint was dry (approximately 24 h of drying time). In Fig. 3(b), cavitating flow over the cylinder can be seen with the painted sample plate beneath it. We tested this paint with different cavitation conditions and did not see any dissolving or detaching of the paint; only cavity collapses led to its removal, which was visually verified (explained in Section 3.2). It should be noted that the paint test is a proxy for actual (metal) erosion. It is a binary technique, as the paint is either removed or not. Therefore, it is a qualitative approach to determine which regions are more prone to erosion. However, from the paint removal pattern over time, it is possible to detect the areas at which the erosion initiates and observe how it is developed, as will be demonstrated later.

The thickness of the paint is measured by a digital microscope (KEYENCE VHX-700F), as shown in Fig. 4(a). This digital microscope uses fine changes in the texture to calculate height data using multi-focal plane microscopy. This means that a 3D image can be created by compiling images captured at different focal planes. In Fig. 4(b), the thickness (approximately 48 μm) of the paint is shown. The paint removal in Fig. 4(b) is obtained by a simple scratch on the plate before the test. The green curve in the plot shows the reference measurement and the red curve shows the actual measurement.

3. Results

In this section, we present the cavitation erosion at three different cavitation numbers together with the corresponding cavity pattern. For further understanding of the flow physics as well as the bluff body effect, the same tests have also been performed in the test-rig, but without any bluff body in the channel throat. Details of different test conditions are given in Table 1. In this table, the non-dimensional numbers are based on the average velocity at the channel throat (u_{th}), the average downstream pressure (p_2), and the cylinder diameter (D) as the reference values. The first three tests NC1, NC2, and NC3 have been done without the cylinder, while the cases C1, C2, and C3 are related to erosion tests with the cylinder. The no-cylinder (NC) cases have been set in a way to have similar inlet pressure and pressure drop as the corresponding with-cylinder (C) cases. As reported in Table 1, the inlet pressure (p_1) and pressure loss over the test section (Δp) in cases NC1, NC2, and NC3 are very similar to the corresponding values in cases C1, C2 and C3, respectively. It will be seen later that the sheet cavity length for each NC case is comparable to the fixed cavity length of the corresponding C case. Furthermore, as seen in the table, both cavitation and Reynolds numbers change between the test cases. The changes in σ are expected to be more prominent, as Re is always in the range of 1.7–2.4 $\times$ 10^5.

[2] The Wilson super ink is used to paint tennis rackets and polyester and usually lasts a few years.

3.1. Flow blockage

The experiments are designed so that the pressure drop is as similar as possible (with and without cylinder), as this has the largest effect on the cavitation number. Due to flow blockage effects, this means that the volume rate can not be the same as well. To investigate the cylinder blockage effect and compare it with the cavity blockage effect, the pressure loss coefficient, K, for the two sets are plotted against the cavitation number in Fig. 5. Here, the pressure loss coefficient is defined as

$$K = \frac{\Delta p}{\frac{1}{2}\rho u_{th}^2}. \tag{2}$$

In the figure, the three leftmost points on each line represent the reported cases in Table 1. The plot lines simply connect the measured points to demonstrate the trend and the error bars show the measurement uncertainty. The errors are estimated based on the measurement uncertainties of the flowmeter and pressure transducers. When we remove the bluff body, the flow is almost cavitation free (assessed by flow visualization) until very low cavitation numbers ($\sigma < 0.6$). However, with the cylinder, the flow cavitates even at relatively high cavitation numbers ($\sigma = 1.16$), as also reported earlier by Ghahramani et al. [37]. In Fig. 5, it is observed that for the bluff body cases (solid black line), by decreasing the cavitation number (increasing the Reynolds number), the pressure loss has a slight reduction at first as the boundary layer momentum thickness decreases. Then there is a sharp drop with a minimum value at $\sigma = 0.64$ (corresponding to case C1), which is due to the lubrication effect of the vapor: in this area, the generation and shedding of cavitating vortices reduce the effective fluid viscosity and friction loads on the body (see Ref. [37] for a detailed description of cavity dynamics). By further decreasing the cavitation number below $\sigma = 0.64$, the pressure drop increases substantially. For such cases, the cavity structures in the cylinder wake are large enough to significantly narrow the effective channel cross-section, and the pressure loss over the channel increases. For the test series without the cylinder (red dashed line), in the cavitation free regime, by decreasing the cavitation number (increasing the Reynolds number), the pressure loss has a slight reduction, similar to the bluff body case. After $\sigma = 0.6$, we first have a slight increase in pressure drop. At $\sigma = 0.575$ (not listed in Table 1), only a sheet cavity with a length of about 7 mm ($1.4D$) is observed on the lower wall, which does not have a considerable volume as compared to the other cases. Then by further decreasing the cavitation number below 0.504, there is a sharp increase in pressure drop similar to the bluff body case. By comparing the two plots and the vertical distance between them (which shows the cylinder blockage effect), we can conclude that the cavitation blockage effect is significant. If we compare the vertical distance between points NC1 and NC3 (or C1 and C3), with the vertical distance between the two plots, it can be stated that for the lowest cavitation number, the blockage effect is about 80% of the blockage effect for the rigid bluff body. However, this is the sum of 'true' blockage (reduced channel cross-section) and cavitation-induced reduction of cross-section.

3.2. Test cases with cavitation erosion

In this section, we investigate cavitation erosion on the test sample with and without the bluff body. In Figs. 6–8, the paint removal results for the test series without cylinder are shown. To understand the related phenomenon in each case, a snapshot of the cavitating flow is also represented. The origin of the horizontal axis, coinciding with the axial/streamwise direction, is set at the start of the sample plate. The axial location (X) is made dimensionless using the length of the sample plate (L). As the vertical axis is not used (as will be discussed later), its origin is set arbitrarily. Without the bluff body, the flow cavitates on the sidewalls and sometimes on the upper wall, in addition to the zone of

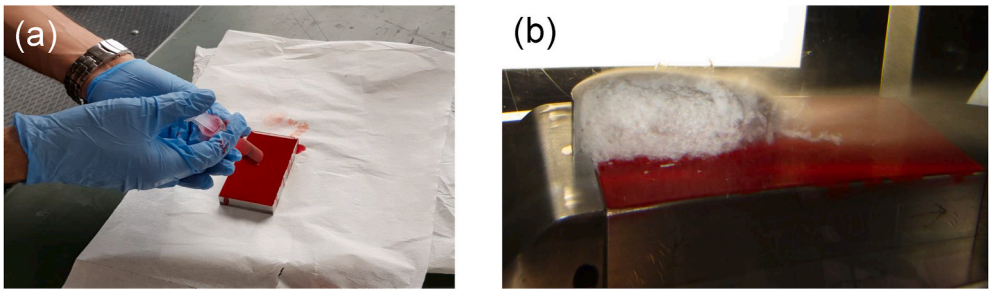

Fig. 3. (a) Applying paint on the sample. The sample was leveled for uniform distribution of paint. The paint was used straight from the source, without any preparation (e.g., shaking, heating, etc). (b) A photograph of the channel showing cavitation on the sample.

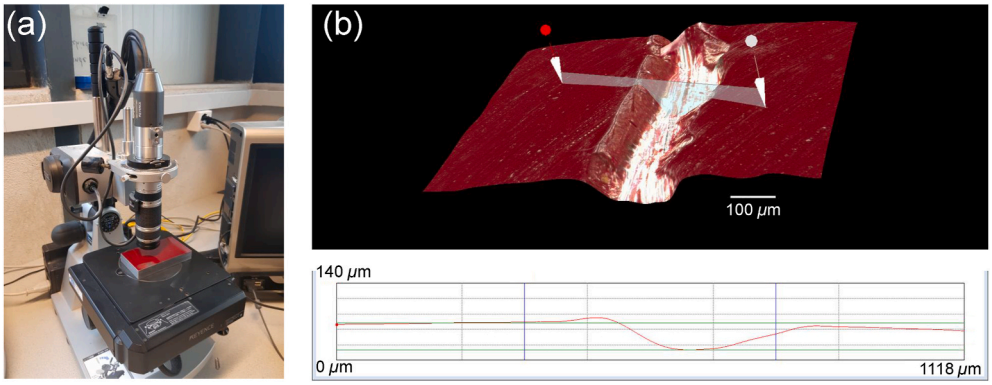

Fig. 4. (a) Paint thickness is measured via a digital microscope (KEYENCE VHX-700F). (b) 3D reconstruction of the paint layer. A scratch (white region) is used to determine the layer thickness. The bottom shows the height profile between the two markers. Thickness of paint is approximately 48 μm. See text for details.

Table 1
Test cases.

No.	$p_1(bar)$	$Q(m^3/s)$	$\Delta p(bar)$	Re ($\times 10^5$)	σ
NC1	3.37	0.0462	0.434	1.71	0.504
NC2	4.26	0.0527	0.602	1.95	0.485
NC3	6.22	0.0643	1.085	2.38	0.458
C1	3.36	0.0408	0.441	1.51	0.641
C2	4.25	0.0471	0.608	1.74	0.604
C3	6.22	0.0582	1.068	2.15	0.559

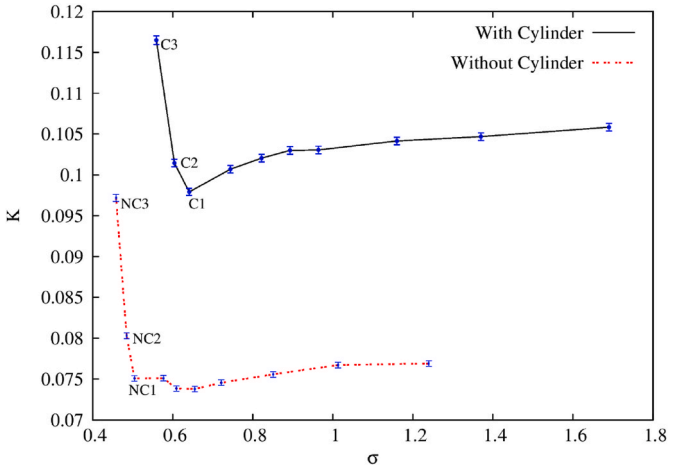

Fig. 5. Pressure loss coefficient (K) versus cavitation number for different test cases with and without the bluff body.

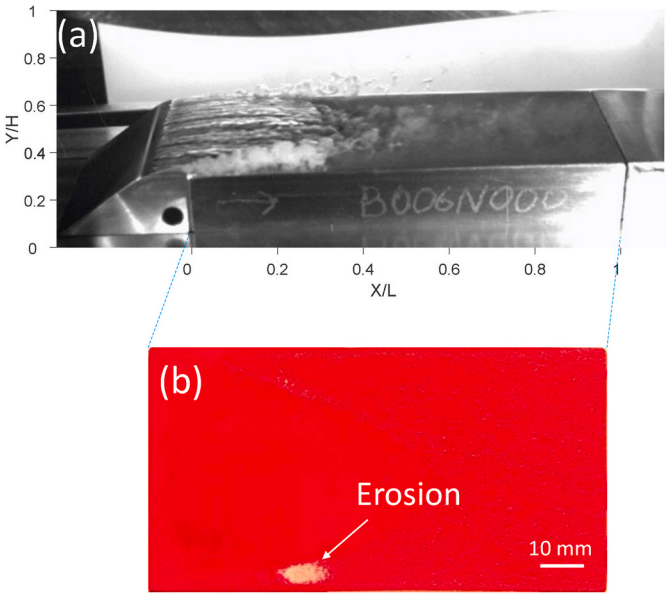

Fig. 6. Case NC1, $\sigma = 0.504$. (a) Cavitation pattern. Flow is from left to right. (b) (Top view of the sample plate) Paint removal after 40 min.

interest, the bottom plate. The sidewall cavities block the observer view considerably. When the flat plate and bottom ramp are mounted on the test-rig, there are always very small but unavoidable gaps between them and the sidewalls. During the test, some liquid penetrates into these gaps. Vortices are created at these gaps as the liquid exits the gaps and the low pressure cores of these vortices induce cavitation on the sidewalls. Because of this obstruction, it is not possible to have a comprehensive analysis of the phenomenon for the no-cylinder cases.

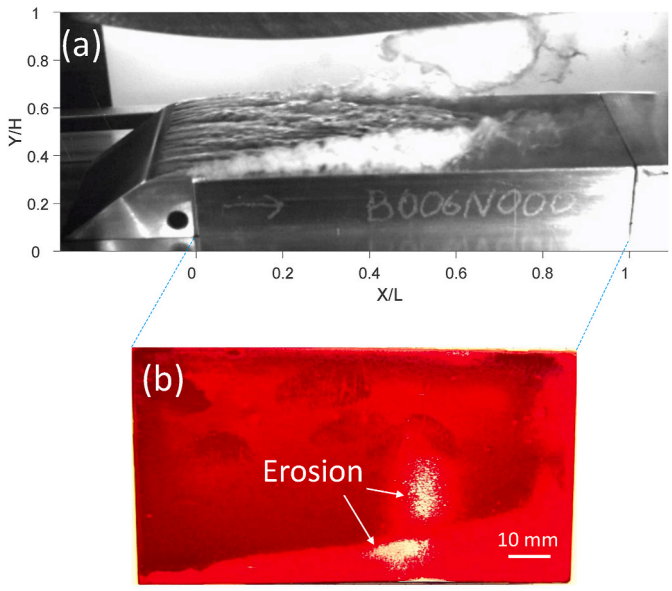

Fig. 7. Case NC2, $\sigma = 0.485$. (a) Cavitation pattern. Flow is from left to right. (b) (Top view of the sample plate) Paint removal after 40 min.

Nevertheless, the cavitation regime and its consequent erosion are still feasible to study. Close to the top wall, some vapor clouds are observed once in a while, and their size grows by decreasing the cavitation number. On the lower wall, however, we have attached cavities whose forms vary between the different cases.

The attached cavity usually occurs when a wake or a region of separated boundary layer fills with vapor. However, sometimes the cavities may occur as 'streaks' of cavitation on the surface. In this type, the formed structures are characterized by the presence of long finger-like cavities, which have a three-dimensional character, and a transverse instability is present. The cavity pattern for $\sigma = 0.458$ (Fig. 8(a) and (b)) is of this type, which is similar to the streak cavitation on the surface of a biconvex hydrofoil reported earlier by Arakeri [43]. Here, by transverse instability, we mean that sometimes, each of the finger-like structures may collapse and re-cavitate irregularly. Also, despite a transverse periodicity, the streaks are not equidistant. According to Arakeri [43]; these cavities start from the expansion of nuclei that most probably come from the freestream. The transverse position of these macroscopic cavities was probably influenced by the presence of small disturbances at the leading edge. Besides, from the transverse periodicity, it can be assumed that the expansion of the flow in the stream tubes containing cavities leads to an increase in the fluid pressure between these tubes. Hence, this phenomena inhibits further lateral spreading of the cavitation [14]. For the growth of cavitation nuclei to macroscopic size, the residence time of these nuclei in the low-pressure area should be long enough, and sometimes this residence time is too short for the formation of streak cavities. In such cases, the attached cavity may occur in separated boundary layers or a mix of boundary layer and nucleate streak separation. In fact, the cavity patterns for $\sigma = 0.485$ and 0.504 seem to be of this type. For $\sigma = 0.504$, we see a rather stable sheet cavity full of vapor, which has some small finger-like structures in between. A similar type of sheet cavitation was reported in the ship propellers by Peters et al. [44]. Sheet cavity was developed at the leading edge of the propeller blade, which results in erosion. For $\sigma = 0.485$ the cavity is more unstable and there is a shift towards the streak type. For a more clear understanding of the explained cavitation regime, it is suggested to look at the corresponding movies (S1–S3), provided as supplementary material to this paper.

The most cavitation erosion takes place in Case NC3, which is the most cavitating as well (i.e. this has the largest cavity in the images). Cavity streaks are quite unstable in this case, and the streak length has significant variations with time. It happens quite frequently that a cavity streak starts to develop, and before it reaches its maximum length, another streak starts at the same place (see movie 'S3'). The length fluctuates, but never exceeds the sample plate. Occasionally, the cavity length only covers half the plate. In Fig. 8(a) and (b), two instances of the flow are shown to illustrate the maximum length of two visible streaks. Furthermore, it is seen that sometimes a part of the cavity detaches at the end of the streak, moves downstream, and collapses before completely passing the sample plate. This collapse occurs in the same region as where the paint is removed. Although the sidewall cavity obstruction prohibits a clear view of the process, it seems that the erosion happens from the fast and aggressive collapse of the cavities shed from the end of the streak, as these vapor clouds are still close to the plate before the collapse. The least aggressive case is NC1, in which the attached cavity originates more from the boundary layer separation, and only a few small streaks are seen in the rather stable sheet cavity. Here, only a little paint is removed at the lower side of the sample plate (Fig. 6 (b)), which is caused by the sidewall cavity. The sidewall cavities are not the same on both sides (as the small gaps between the tunnel and the test plate are uncontrollable and asymmetric), and it can cause a little asymmetry in the cavity closure line. Finally, in case NC2, we see two regions of paint removal on the sample (Fig. 7(b)), one close to the lower edge due to the side cavity, and another one located almost in the middle of plate width, but with a little deviation towards to the lower edge. This asymmetry, which is thought to be due to sidewall cavities, as well as the visualization limits, were among the main motivations in using a bluff body for erosion study, as will be discussed later. Case NC2 is the most challenging one in this series to analyze since the cavity streaks are attached to each other and there is no transverse space between them (contrary to what we see for case NC3). As a consequence, it is more difficult to estimate their unsteady behavior distinctly. However, considering the fact that there are more and larger streaks in this case, as compared to NC1, and from a comparison between cases NC1 and NC2, it can be assumed that the paint removal at the cavity closure line is caused from the collapse of streak cavities.

As described in the previous section, erosion measurements were also performed with the inclusion of the bluff body. The last three cases of Table 1 ($\sigma = 0.641, 0.604, 0.559$) represent the flow over a bluff body. Based on the earlier studies in literature and previous experience at ANDRITZ Hydro, we chose these cavitation numbers for the bluff body, which are higher compared to the no-bluff body cases because the cavitation and induced erosion are achieved earlier due to the bluff body effect, as explained in section 1. By investigating the flow dynamics in a previous study [37], we found that for cases C1, C2 and C3, a large vapor structure is attached to the bluff body as a fixed cavity and the streamwise velocity component inside this fixed cavity is negative, i.e. in the upstream direction. Also, an upstream moving disturbance jet appears in the fixed cavity, which accelerates the reverse flow towards the cylinder. It also affects the cavity dynamics significantly, causing its detachment from the cylinder and perturbing the liquid-vapor interface. In Fig. 9, a schematic overview of the cavitating flow over the bluff body is shown. The cavitating flow is schematically visualized for three different cavity lengths. This figure is an approximation of the cavity behavior observed in the images. It can be seen that with decreasing cavitation number, the cavity length increases at the time of detachment. At the cavity closure, most of the vapor cavities collapse and result in erosion on the sample plate (explained in more detail in the later paragraph). When the cavity detaches, it also sheds vortex cavities downstream. At the front of the cylinder base, a horseshoe cavity can be seen. This horseshoe cavity is also a cause of erosion around the cylinder base (as will be discussed later).

In Fig. 10, a time series of a test case (C1) with $\sigma = 0.641$ is shown together with the erosion pattern (Fig. 10(e)). It is clear from the snapshots that the shedding and deformation at the closure of the cavity takes place sooner as compared to the cases discussed without the bluff body. In Fig. 10(b) and (c), the development and detachment of a vortex

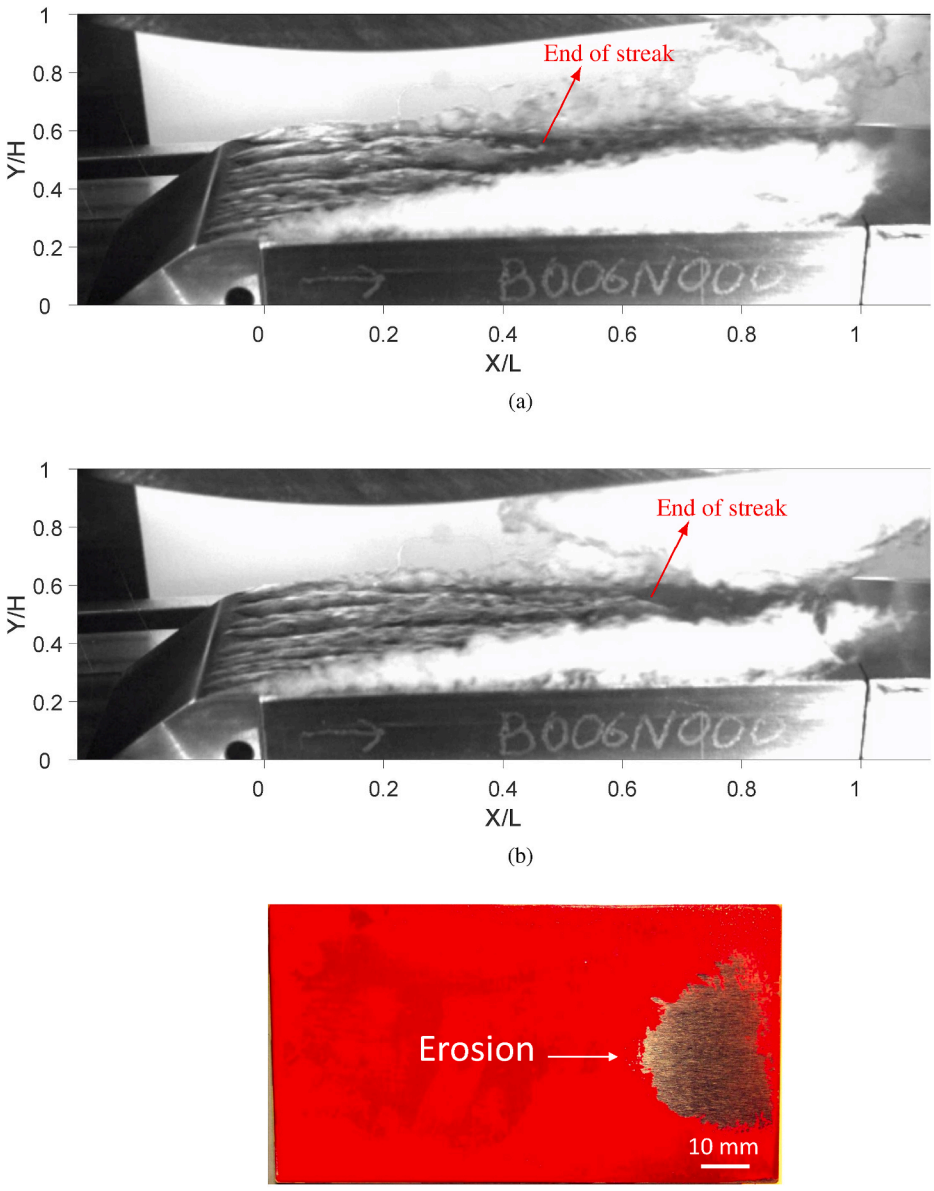

Fig. 8. Case NC3, $\sigma = 0.458$. (a–b) Two examples of cavitation patterns to show the variation in streak length. Flow is from left to right. (c) (Top view of the sample plate) Paint removal after 40 min.

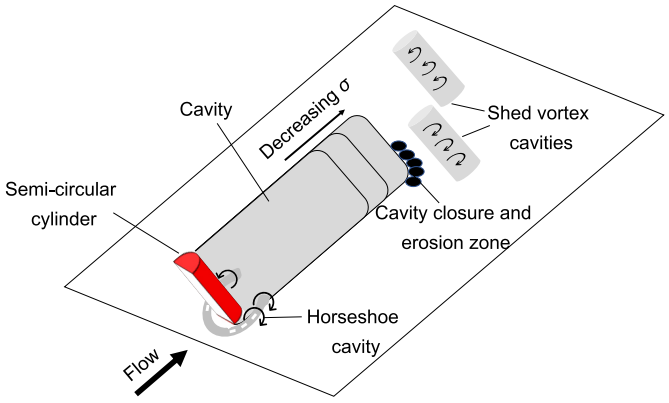

Fig. 9. A schematic overview of the cavitating flow over a semi-circular cylinder. Drawing not at scale for clarity.

can be seen at the closure of the cavity (indicated with red arrows). The rest of the cavity is attached to the cylinder. The figure shows a time series of the flow with $\Delta T = 4 \times 10^{-5}$ s. At $T_0 + 9\Delta T$, a reverse flow can be seen together with the rolling of the cavity (indicated by the blue arrow). The front of the reverse jet is depicted by a red arrow. A detailed description of the dynamics of this reverse jet is provided in the earlier study [37]. The reverse flow of the cavity has an angle towards the bottom plate. It moves further upstream ($T_0 + 14\Delta T$) and finally hits the cylinder ($T_0 + 22\Delta T$). Moreover, one more interesting characteristic of this flow is the horseshoe cavity formed just in front of the cylinder base. The horseshoe cavity is indicated by the green inclined arrow and it can be seen more clearly in the enlarged view (Fig. 10(a)). The horseshoe cavity is more clear in motion (supplemental movies). The periodic collapse of this horseshoe cavity causes erosion just downstream of the cylinder and this erosion will also be observed in the cases discussed later. In the erosion pattern (Fig. 10(e)) it can be seen that most of the eroded part is around the perimeter of the cavity, both at the end as well as the sides. In this case, erosion is not just attributed to the collapses at

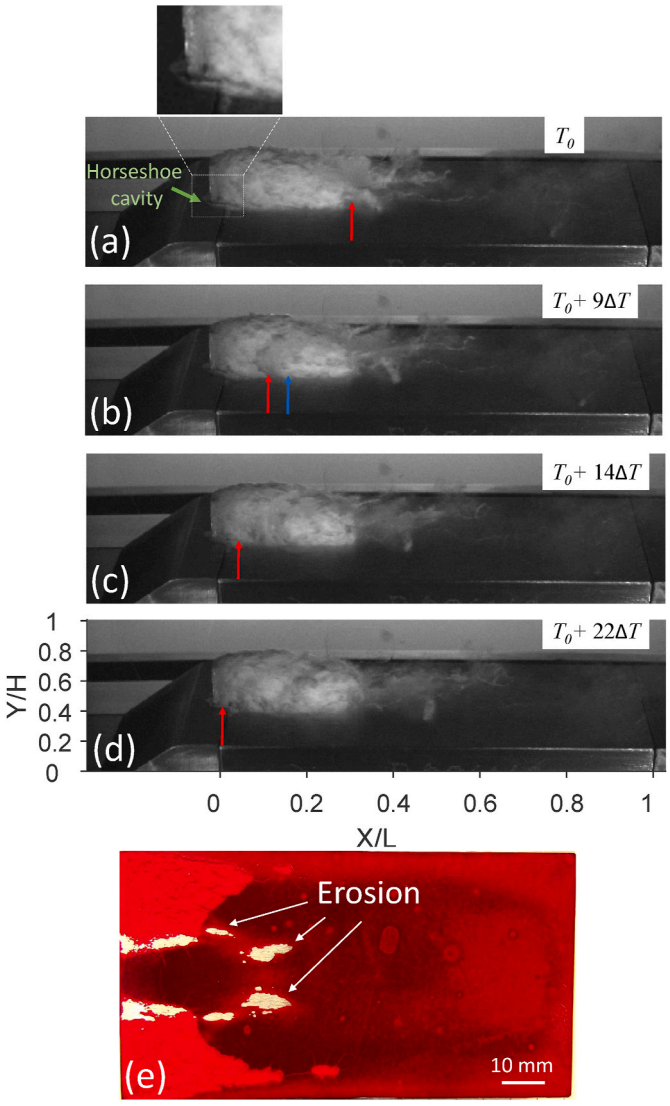

Fig. 10. Case C1, $\sigma = 0.641$. (a–d) A time series of cavity collapse, the red arrow locates the front of the reverse jet. The rolling of the cavity is indicated by the blue arrow. The supplementary movie 'S4' more clearly shows these features. Flow is from left to right. (e) (Top view of the sample plate) Paint removal after 40 min. (For interpretation of the references to colour in this figure legend, the reader is referred to the web version of this article.)

the trailing edge of the cavity, clear erosion can be seen around the cavity too. The reason for this might be because of the length of the attached cavity, which is not very long in this case as compared to C2 and C3 (to be discussed later). Because of a shorter attached cavity, the reverse flow occurs more frequently in this case, as it reaches the bluff body faster. Due to this reverse flow, we see collapse happening at the bottom of the cavity (towards the sample plate), which results in the removal of paint. In supplementary data, three movies (S4–S6) can be found corresponding to the bluff body cases that further illustrate the cavitation regimes.

By reducing the cavitation number to $\sigma = 0.604$ or lower, most of the cavity remains attached to the bluff body. Only small structures are shed downstream from the attached part. In Fig. 11(a) and (b), two snapshots of the cavity structures of case C2 ($\sigma = 0.604$) are presented to illustrate some features of the flow. The cavity length increases compared to case C1. The shedding area of the vapor bubbles from the trailing edge is relatively smaller than the attached cavity in this case. After 40 min of operation, the main erosion took place at the closure of the cavity. Here the length of the attached cavity increases and the shed vapor clouds also increase in size, which makes their collapse more violent. The more aggressive collapse will in turn result in more erosion. The eroded part is shown in Fig. 11(d). It can be seen that the downstream area of the eroded part is increased compared with the earlier case. This will be further confirmed in the next case. However, in this case we do not see erosion around the sides of the attached cavity. In Fig. 11(c), at the start of the sample plate (just downstream of the bluff body), we see two clear erosion spots. After a careful examination of the high-speed movies, we find that a horseshoe cavity is generated in front of the cylinder base and collapses, similar to case C1 (Fig. 10(a)). That horseshoe cavity extends until this eroded part. This phenomenon is further explained in the next case. It is worth mentioning that the erosion pattern in this case is very similar to the one reported by Escaler et al. [35]; who performed erosion tests on four different materials and at a similar flow speed. They found that the wear is mainly located in two elliptical areas in the first half, nearest to the cylinder, immediately behind the obstacle for all the sample plates of different materials. Cavitation erosion is strongly concentrated in the center of each region and diminishes gradually towards the border. In the downstream half of the samples, a few isolated, relatively large impacts can also be observed. Escaler et al. [35] concluded that the region where collapses take place appears gradually from the first hours and no sudden increase of damage is observed during the run. Qualitatively our erosion patterns are very much similar to those cases, which means that the test times can be significantly reduced from 75 h to 40 min. The tests are compared further in the next section.

In Fig. 11(c), the beginning of erosion development for this case can

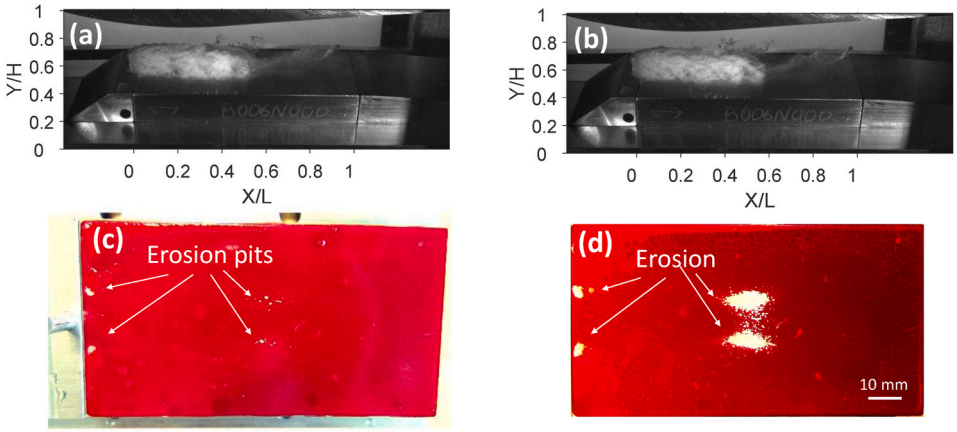

Fig. 11. Case C2, $\sigma = 0.604$. (a–b) Two snapshots of cavity collapse. Flow is from left to right. (c) (Top view of the sample plate) Beginning of erosion development. (d) Paint removal after 40 min.

be seen. The sample plate was taken out of the test-rig after approximately 15 min of operation. We can see a few erosion pits developing at the main erosion location together with the erosion just downstream of the bluff body. With time these pits become bigger.

A third case C3 is selected by further decreasing the cavitation number to $\sigma = 0.559$. In Fig. 12(a), a snapshot of the cavity can be seen. The cavity region extends almost to the end of the sample plate. The intensity of cavitation increases considerably compared with Cases C1 and C2, and larger vapor structures are shed from the cavity, which makes the collapses very violent. We also see the development of small and intermittent sidewall cavities. Similar to the earlier cases, we have reverse flow inside the attached cavity, but it occurs less frequently as the fixed cavity is longer. In Fig. 12(b), the corresponding erosion pattern for case C3 can be seen. The downstream of the sample plate shows a larger eroded area compared to the earlier cases, as expected. Some paint removal also took place at the start of the sample plate. Similar to the earlier cases, this is assumed to happen due to the horseshoe cavity collapse in front of the cylinder. The horseshoe cavity is indicated by the green inclined arrow and it can be seen more clearly in the enlarged view (Fig. 12(a)). Horseshoe cavity implosion is very important due to its aggressiveness. Dular and Petkovšek [11] also showed the destructive behavior of a horseshoe cavity collapse on a foil. At the sides of the sample plate, some narrow erosion can also be seen due to the unavoidable sidewall cavity (indicated by the white arrows in Fig. 12(b)). This case is the most aggressive and violent compares to the previous cases which ultimately results in more removal of the paint. The largest paint removal at the end of the sample looks similar to the paint removal pattern from no-cylinder case NC3, which is expected, as both of them happen from the violent collapse of large vapor clouds at the same region.

4. Discussion

This study has analyzed the erosion (paint removal) caused by different cavitation mechanisms at various cavitation numbers. We observed more erosion for the cases with the bluff body, as compared to the cases without the bluff body. All six cases investigated in this paper are shown in Fig. 13. Left panels (a-c) belong to the cases without the bluff body and right panels (d-f) belong to the cases with the bluff body. The inclusion of the bluff body has an obvious effect on erosion. The cavitation numbers were adjusted for the bluff body cases (higher cavitation numbers). For cases with the bluff body, to cause erosion, we need less power into the system. In cases NC3 (Fig. 13(c)) and C3 (Fig. 13(f)) the cavity lengths were longer than other two cases. In Fig. 13(f), the erosion at the start of the plate is caused by the horseshoe cavity induced by the base of the bluff body. This horseshoe cavity is absent in the case NC3. Furthermore, with the bluff body the erosion pattern downstream has a shape corresponding to the body, as we can see two lobes caused by the recirculating character of the flow at the end of the attached cavity. However, in case NC3, the erosion is mainly caused by the streak cavities formed at the ramp upstream of the section, as we can see one lobe around the end of the streak cavities at their maximum length. For the cases NC2 and C2, the patterns are pretty similar to the aforementioned cases, however, the eroded area is smaller. It is also important to mention here that the case NC2 is less stable because of the asymmetry in the cavitating flow. In this case, most of the erosion is caused by the streak cavities which seem to be caused by tiny impurities upstream in the geometry. When the streaks are caused by uncontrolled impurities (in the liquid or on the walls) then we do not have control of the situation and comparing erosion tests over time will be impossible. Case NC2 is less repeatable and it seems to be due to the flow asymmetry and uncontrollable streak cavities. The tiny impurities on the lower wall, in a way, represent small bluff bodies. Lastly, the most interesting cases to compare are NC1 and C1. For NC1, we saw no erosion even after running the test for 2 h, which means the cavity was not aggressive enough to cause erosion. It should be noted that the paint removal at the lower side of the sample plate in Fig. 13(a) is caused by the sidewall cavity (explained in Section 3.2). For case C1, the erosion pattern is very distinct. Most of the erosion takes place around the perimeter of the cavity.

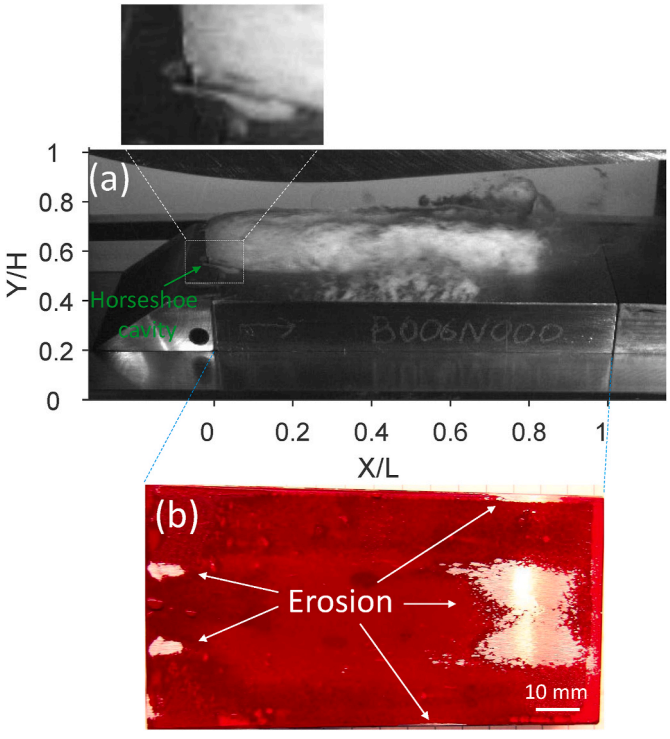

Fig. 12. Case C3, $\sigma = 0.559$. (a) Cavitation pattern. Flow is from left to right. (b) (Top view of the sample plate) Paint removal after 40 min.

Fig. 14 systematically shows the cavity and erosion lengths plotted against the cavitation number. The cavity length for no-bluff body cases cannot be measured properly as the sidewall cavity blocks the optical view. The cavity length for the cases with the bluff body are measured after averaging the frames. The length is non-dimensionalized with the diameter of the cylinder. Complete details of this procedure can be found in the earlier paper by Ghahramani et al. [37]. In the plot, the bars represent the width covered by the paint removal in the streamwise direction (end of the attached cavity). The erosion patterns for the cases C2 and C3 follow the cavity length, as this is where the collapse of the cavity takes place. For case C1, the erosion does not only take place at the collapse area but also around the perimeter of the cavity (as discussed earlier).

The comparison of our study with earlier studies is critical, as we have successfully managed to reduce the operation time of the experiment. Escaler et al. [36] investigated cavitation erosion on different materials using semi-circular cylinders, as shown in Fig. 15(a). The authors ran the experiment for 75 h to obtain these results. In Fig. 15(b), the cavitation erosion pattern for case C2 can be seen after approximately 40 min of operation. A good qualitative agreement is found between the downstream paint removal and erosion pattern by Escaler et al. [36] after comparing these two studies. It should be mentioned that the semi-circular cylinder used by Escaler et al. [36] had very similar dimensions to the current test (5 mm in diameter and 10 mm in height) and the inlet velocity was 35 m/s which corresponds to a Reynolds number of 1.75×10^5, similar to the corresponding value for case C2. However, the current study's cavity length is larger than the one reported by Escaler et al. [36]; which causes erosion to take place further downstream.

Fig. 16 shows the result of an earlier test at ANDRITZ Hydro to measure the mass loss using the stainless steel and in the current test-rig. The test was performed at a flow velocity of 50 m/s ($Re = 2.5 \times 10^5$). In

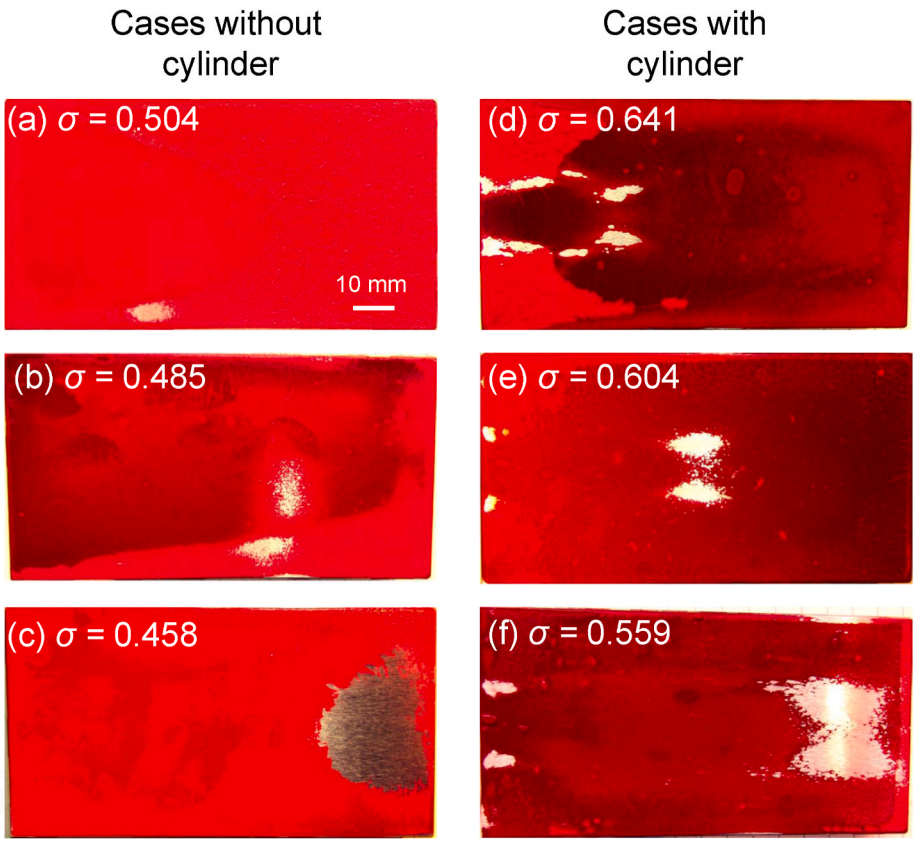

Fig. 13. An overview of erosion patterns at various cavitation numbers. (a–c) Test sample plates representing cavitation erosion for cases (NC1, NC2 and NC3) without the bluff body. (d–f) Test sample plates representing cavitation erosion for cases (C1, C2 and C3) with the bluff body. These are top views of the sample plate.

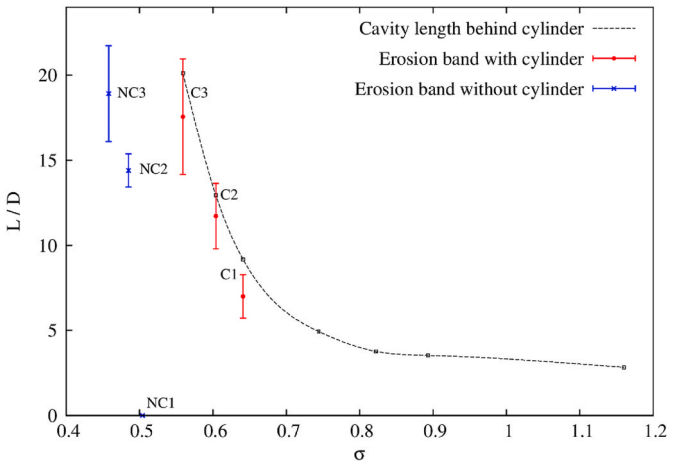

Fig. 14. Cavity length and erosion width along the plate length, as a function of cavitation number; all values are normalized by the cylinder diameter.

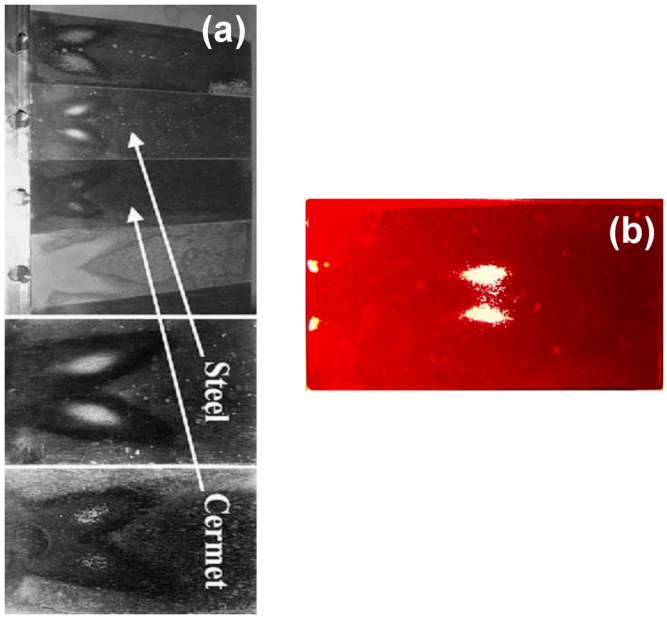

Fig. 15. (a) Cavitation erosion tests on cermet and stainless steel sample plates after 75 h test. Reproduced from Escaler et al. [36] with permission © 2003 Elsevier. (b) A cavitation erosion photograph (top view) of case C2 after a test of 40 min.

the old test, the cylinder was placed on the sample plate (hole in Fig. 16), while in the current experiments, the cylinder was placed before the sample plate. The figure shows the erosion pattern after 30 h of operation. After this time, 26 mg loss of mass was found, where the total mass of the sample plate was 615.788 mg. The global material loss pattern looks qualitatively similar to the paint removal of case C1, with two erosion spots downstream and two thin lines connecting the cylinder with the main erosion spots. These thin lines follow the cavity contour. However, these lines are not present in case C2. The difference can be associated with surface alteration in the metallic surface compared to the painted surface. Also, metallic structures are quite sensitive to surface alterations. An additional factor is a large difference in the operation time of the experiment. The overall agreement is good, considering the slightly different flow conditions.

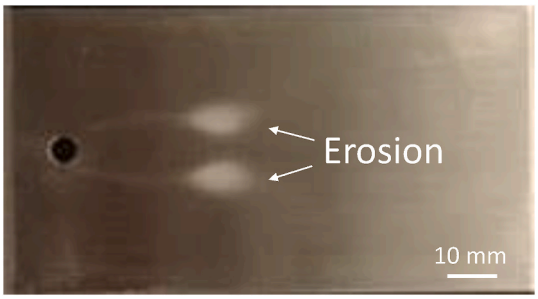

Fig. 16. (Top view of the sample plate) Mass loss (erosion) pattern on stainless steel at a flow velocity of 50 m/s ($Re = 2.5 \times 10^5$).

In summary, Figs. 15 and 16 provide qualitative verification of the paint removal tests for cases C1 and C2, while Fig. 13 is a summary of the various erosion patterns for the cases with and without cylinder and for various cavitation numbers.

5. Conclusions

The purpose of the current study was to investigate the erosion caused by cavitation induced with and without an obstacle. We explained the differing collapsing behavior of cavitation, which leads to erosion in the two groups of cases. An experimental investigation was performed in a channel with a semi-circular cylinder obstacle. Cavitation was achieved by employing a range of pressure differences over the test section. The obstacle promotes and localizes cavitation-induced erosion. The flow field behind the semi-circular cylinder was investigated as a characteristic example of bluff bodies that exhibit a distinct, separated vortex flow in their wake. A high-speed camera documented the cavitation behavior. At the same time, erosion tests were performed using paint (stencil ink). The intensity of cavitation is described by the cavitation number (σ); the lower the cavitation number, the higher the cavitation intensity. From this study, the following conclusions can be formulated:

- It was seen that the cavitation can alter the flow field considerably and flow blockage caused by the large cavities is in the same order as the blockage effect by the rigid bluff body.
- Based on the results, three erosive cases (C1, C2, and C3), at different cavitation numbers were identified with the bluff body and two erosive cases (NC2 and NC3) without the bluff body. The erosion results are summarized in Fig. 13. The erosion (removal of paint) after 40 min of operation revealed distinct results. It was seen that with the increase in cavitation intensity, the erosion area increases. The collapses from the cavities get very violent as the large vapor structures are shed from the cavity. We also see the development of the sidewall cavity for the no-bluff body cases.
- In the cases NC2 and NC3, most of the erosion seemed to be caused by streak cavities, which develop upstream, while no paint removal is seen when the cavity is generated from boundary layer separation, case NC1.
- The bluff body obstacle promotes and localizes cavitation-induced erosion on the sample plate compared to the cases without the bluff body. This ultimately means that in the cases with the bluff body, less power is required in the system to cause erosion. The erosion patterns caused by the bluff body cavitation are more repeatable compared to the cases without the bluff body due to the localized cavitation load.
- It was also concluded that the erosion patterns for the cases C2 and C3 appear near the collapse of the cavity. For case C1, the erosion takes place at the collapse area and around the perimeter of the cavity. The reason for the multiple erosion locations is mainly because of frequent collapses due to small cavities and well as more frequent reverse flow in the attached cavity.

We demonstrate that paint tests, combined with this geometry, provide an efficient and economical way to investigate erosion patterns compared to expensive material loss tests. The comparison of our study with earlier studies revealed that the use of paint tests, combined with this geometry, could significantly reduce the operating time (and thus costs) by one or two orders of magnitude (here 75 h to 40 min) as running such a test-rig is very expensive.

Despite an extensive available collection of experimental studies on cavitation (as discussed in Section 1), studies that link cavitation to erosion are limited. In this study, we are also able to identify the erosive cavitation mechanisms and structures: horseshoe cavity (present at the cylinder base), streak cavitation and bubble collapses at the closure of cavity. These results may serve as validation data for numerical studies in the future. In addition, paint studies could also be used to monitor erosion progression if a camera and illumination are optimized to image the sample plate (provided that the flow can temporarily be reduced to avoid cavitation during imaging).

Declaration of competing interest

The authors declare that they have no known competing financial interests or personal relationships that could have appeared to influence the work reported in this paper.

Acknowledgments

This work is funded through the EU H2020 Grant 642536 ‘CaFE’ (SJ, EG) and ERC Consolidator Grant 725183 ‘OpaqueFlows’ (SJ, CP). The authors wish to express their gratitude to Dr. Etienne Parkinson and Dr. Jean-Christophe Marongiu and all laboratory technicians and researchers at ANDRITZ Hydro (Switzerland) for hosting Ebrahim Ghahramani and Saad Jahangir in a two-month research visit as a part of the CaFE project. We also specially thank Mohammad Hossein Arabnejad (Chalmers) and Ali Amini (EPFL) for their suggestion regarding the stencil ink for the paint tests.

Appendix A. Supplementary data

Supplementary data related to this article can be found at https://doi.org/10.1016/j.wear.2021.203917.

References

[1] M. Gavaises, D. Papoulias, A. Andriotis, E. Giannadakis, A. Theodorakakos, Link between Cavitation Development and Erosion Damage in Diesel Injector Nozzles. Technical report, SAE Technical Paper, 2007.
[2] J. Hunt, A. Ryde-Weller, F. Ashmead, Cavitation between meshing gear teeth, Wear 71 (1) (1981) 65–78.
[3] C. Arn, F. Avellan, P. Dupont, Prediction of francis turbines efficiency alteration by travelling bubble cavitation, in: Proceedings of the19th IAHR Symposium on Hydraulic Machinery and Cavitation, vol. 1, International Association For Hydraulic Research, Singapore, Republic of Singapore, 1998, pp. 230–235.
[4] R. Hirschi, P. Dupont, F. Avellan, J.-N. Favre, J.-F. Guelich, E. Parkinson, Centrifugal Pump Performance Drop Due to Leading Edge Cavitation: Numerical Predictions Compared with Model Tests, 1998.
[5] B. Niemczewski, Observations of water cavitation intensity under practical ultrasonic cleaning conditions, Ultrason. Sonochem. 14 (1) (2007) 13–18.
[6] M. Wan, Y. Feng, G. ter Haar, Cavitation in Biomedicine, vol. 23, Springer, 2015.
[7] M.S. Plesset, R.B. Chapman, Collapse of an initially spherical vapour cavity in the neighbourhood of a solid boundary, J. Fluid Mech. 47 (2) (1971) 283–290.
[8] W. Lauterborn, H. Bolle, Experimental investigations of cavitation-bubble collapse in the neighbourhood of a solid boundary, J. Fluid Mech. 72 (2) (1975) 391–399.
[9] M. Dular, O.C. Delgosha, M. Petkovšek, Observations of cavitation erosion pit formation, Ultrason. Sonochem. 20 (4) (2013) 1113–1120.
[10] T.J. Van Terwisga, P.A. Fitzsimmons, L. Ziru, E.J. Foeth, Cavitation erosion–a review of physical mechanisms and erosion risk models, in: 7th International Symposium on Cavitation, Michigan, USA, 2009.
[11] M. Dular, M. Petkovšek, On the mechanisms of cavitation erosion–coupling high speed videos to damage patterns, Exp. Therm. Fluid Sci. 68 (2015) 359–370.

[12] T. Leighton, The Acoustic Bubble, Academic press, 2012.
[13] D.D. Joseph, Cavitation and the state of stress in a flowing liquid, J. Fluid Mech. 366 (1998) 367–378.
[14] C.E. Brennen, Cavitation and Bubble Dynamics, Cambridge University Press, 2014.
[15] I. Tzanakis, L. Bolzoni, D. Eskin, M. Hadfield, Evaluation of cavitation erosion behavior of commercial steel grades used in the design of fluid machinery, Metall. Mater. Trans. 48 (5) (2017) 2193–2206.
[16] S. Hanke, A. Fischer, M. Beyer, J. dos Santos, Cavitation erosion of nial-bronze layers generated by friction surfacing, Wear 273 (1) (2011) 32–37. Selected papers from 14th Nordic Symposium on Tribology, NORDTRIB 2010.
[17] G. Gao, Z. Zhang, Cavitation erosion behavior of 316l stainless steel, Tribol. Lett. 67 (4) (2019) 1–12.
[18] H. Liu, T. Zhang, C. Kang, Evaluation of cavitation erosion resistance of copper alloy in different liquid media, Mater. Corros. 69 (7) (2018) 917–925.
[19] M. Dular, B. Bachert, B. Stoffel, B. Širok, Relationship between cavitation structures and cavitation damage, Wear 257 (11) (2004) 1176–1184.
[20] B. Ji, X. Luo, R.E. Arndt, Y. Wu, Numerical simulation of three dimensional cavitation shedding dynamics with special emphasis on cavitation–vortex interaction, Ocean Eng. 87 (2014) 64–77.
[21] B. Ji, X. Luo, R.E. Arndt, X. Peng, Y. Wu, Large eddy simulation and theoretical investigations of the transient cavitating vortical flow structure around a naca66 hydrofoil, Int. J. Multiphas. Flow 68 (2015) 121–134.
[22] H. Cheng, X. Bai, X. Long, B. Ji, X. Peng, M. Farhat, Large eddy simulation of the tip-leakage cavitating flow with an insight on how cavitation influences vorticity and turbulence, Appl. Math. Model. 77 (2020) 788–809.
[23] H. Cheng, X. Long, B. Ji, X. Peng, M. Farhat, A new euler-Lagrangian cavitation model for tip-vortex cavitation with the effect of non-condensable gas, Int. J. Multiphas. Flow 134 (2021) 103441.
[24] E. Ghahramani, M.H. Arabnejad, R.E. Bensow, A comparative study between numerical methods in simulation of cavitating bubbles, Int. J. Multiphas. Flow 111 (2019) 339–359.
[25] C. Eskilsson, R.E. Bensow, S. Kinnas, Estimation of Cavitation Erosion Intensity Using Cfd: Numerical Comparison of Three Different Methods, Fourth International Symposium on Marine Propulsors, Texas, USA, 2015.
[26] A. Peters, O. el Moctar, Numerical assessment of cavitation-induced erosion using a multi-scale euler–Lagrange method, J. Fluid Mech. (2020) 894.
[27] E. Ghahramani, M.H. Arabnejad, R.E. Bensow, Realizability improvements to a hybrid mixture-bubble model for simulation of cavitating flows, Comput. Fluids 174 (2018) 135–143.
[28] S. Joshi, J.P. Franc, G. Ghigliotti, M. Fivel, Bubble collapse induced cavitation erosion: plastic strain and energy dissipation investigations, J. Mech. Phys. Solid. 134 (2020) 103749.
[29] M. Van Rijsbergen, E.-J. Foeth, P. Fitzsimmons, A. Boorsma, High-speed video observations and acoustic-impact measurements on a naca0015 foil, in: Proc. 8th Int. Sym. Cavitation, CAV2012, Singapore, 2012.
[30] M. Callenaere, J.-P. Franc, J.-M. Michel, M. Riondet, The cavitation instability induced by the development of a re-entrant jet, J. Fluid Mech. 444 (2001) 223–256.
[31] H. Ganesh, S.A. Mäkiharju, S.L. Ceccio, Bubbly shock propagation as a mechanism for sheet-to-cloud transition of partial cavities, J. Fluid Mech. 802 (2016) 37–78.
[32] S. Jahangir, E.C. Wagner, R.F. Mudde, C. Poelma, Void fraction measurements in partial cavitation regimes by x-ray computed tomography, Int. J. Multiphas. Flow 120 (2019) 103085.
[33] Y. Saito, K. Sato, Cavitation bubble collapse and impact in the wake of a circular cylinder, in: Proceedings of the 5th International Symposium on Cavitation, CAV2003, Osaka, Japan, 2003.
[34] S. Fry, Investigating cavity/wake dynamics for a circular cylinder by measuring noise spectra, J. Fluid Mech. 142 (1984) 187–200.
[35] X. Escaler, F. Avellan, E. Egusquiza, Cavitation erosion prediction from inferred forces using material resistance data, in: Proc. 4th Int. Sym. Cavitation, CAV2001, California, USA, 2001.
[36] X. Escaler, M. Farhat, F. Avellan, E. Egusquiza, Cavitation erosion tests on a 2d hydrofoil using surface-mounted obstacles, Wear 254 (5–6) (2003) 441–449.
[37] E. Ghahramani, S. Jahangir, M. Neuhauser, S. Bourgeois, C. Poelma, R.E. Bensow, Experimental and numerical study of cavitating flow around a surface mounted semi-circular cylinder, Int. J. Multiphas. Flow 124 (2020) 103191.
[38] J.-P. Franc, J.-M. Michel, Fundamentals of Cavitation, vol. 76, Springer science & Business media, 2006.
[39] S. Jahangir, W. Hogendoorn, C. Poelma, Dynamics of partial cavitation in an axisymmetric converging-diverging nozzle, Int. J. Multiphas. Flow 106 (2018) 34–45.
[40] W. Pfitsch, S. Gowing, D. Fry, M. Donnelly, S. Jessup, Development of measurement techniques for studying propeller erosion damage in severe wake fields, in: Proceedings of the 7th International Symposium on Cavitation, CAV2009, Michigan, USA, 2009.
[41] Y. Cao, X. Peng, K. Yan, L. Xu, L. Shu, A qualitative study on the relationship between cavitation structure and erosion region around a 3d twisted hydrofoil by painting method, in: Fifth International Symposium on Marine Propulsors, 2017.
[42] M.H. Arabnejad, A. Amini, M. Farhat, R.E. Bensow, Hydrodynamic mechanisms of aggressive collapse events in leading edge cavitation, J. Hydrodyn. 32 (1) (2020) 6–19.
[43] V.H. Arakeri, Water Tunnel Investigations of Scale Effects in Cavitation Detachment from Smooth Slender Bodies and Characteristics of Flow Past a Bi-convex Hydrofoil, Report No. E-79A.12, 1971.
[44] A. Peters, U. Lantermann, O. el Moctar, Numerical prediction of cavitation erosion on a ship propeller in model-and full-scale, Wear 408 (2018) 1–12.